JOURNAL OF AIRCRAFT
Vol. 43, No. 3, May–June 2006

Studies of Residual Stress in Single-Row Countersunk Riveted Lap Joints

Gang Li,* Guoqin Shi,† and Nicholas C. Bellinger‡
National Research Council Canada, Ottawa, Ontario K1A 0R6, Canada

Variations of stress and strain, from the riveting process through the tensile loading stage in lap joints with a single countersunk rivet, were studied experimentally and numerically. In situ microstrain gauges were used to measure the strain variations during the entire loading sequence. Three-dimensional finite element (FE) models were generated to simulate the experimental setup. The material elastoplastic constitutive relationship and geometric nonlinear properties, as well as nonlinear contact boundary conditions, were included in the numerical simulations. The numerical modeling techniques were validated using the experimental data. The residual minimum principal stress resulting from the riveting process and the maximum principal stress when the joints were in tension, determined from the FE analyses, are presented. The stress variations along a prescribed path are also presented. The aim of the research is to develop an accurate three-dimensional numerical technique to study the residual stress and strain as well as the stress and strain variations that occur during the entire loading history.

Nomenclature

C	=	material parameter
D	=	rivet shank diameter
D_{hole}	=	inner sheet hole diameter
$D_{\max}$	=	maximum rivet shank diameter after riveting
E	=	Young's modulus
H	=	rivet protruding height above inner sheet surface after riveting
H_{o}	=	rivet protruding height above inner sheet surface before riveting
m	=	material parameter
ε	=	normal strain
$\varepsilon_{\text{true}}$	=	true strain
ν	=	Poisson's ratio
σ	=	normal stress
σ_{true}	=	true stress beyond initial yield stress
σ_{y}	=	initial yield stress

I. Introduction

THE residual stress and strain in the hole vicinity induced by the riveting process has a significant effect on the joint fatigue behavior.[1–6] To obtain a better understanding of the fatigue behavior of the fuselage lap joint, it is necessary to investigate the stress and strain variations during the entire loading sequence from the riveting process to the tensile loading stage.

A literature review[1–10] revealed that 1) few experimental and numerical studies cover the entire loading sequence and 2) very few experimental data have been obtained to determine the strain variation that occurs from the riveting process to tensile loading stage. These gaps suggest that more work is required to fully understand the stress and strain variations in joints. A research project is underway at the Institute for Aerospace Research to investigate the residual stress/strain in lap joints.

Because of the complexity associated with the joint riveting process and the tensile loading stage, it is difficult to develop a closed-form theoretical solution to study the stress and strain fields in the vicinity of a hole. Both experimental and numerical methods were used to study the lap joints in this paper. Residual stress distributions were studied using two-dimensional axisymmetric finite element models[11] and experimental testing used both microstrain gauges and a neutron diffraction technique.[7,11–13] To further investigate the effects of residual stress/strain on the stress/strain variations during the tensile loading stage, lap joints with a single countersunk rivet were studied using three-dimensional finite element methods and experimental techniques.

In this paper, three different squeeze forces, 35.59, 44.48, and 53.38 kN (Ref. 14), were used to install the rivets, and then the joints were loaded in tension to a maximum stress of 98.5 MPa (Ref. 9). The main objective of this work was to accumulate experimental data to develop a numerical simulation capability to study the stress and strain states of fuselage lap joints fastened together using countersunk-type rivets and to obtain stress and strain data to study the fatigue life of fuselage lap joints.

II. Experimental Details

A. Specimen Information

A total of three joint specimens were tested. Each lap joint consisted of two bare 2.03-mm-thick 2024-T3 Al alloy sheets riveted with a 2117-T4 Al alloy countersunk-type MS20426AD8-9 rivet.[15] The dimensions of the sheets were $200 \times 38.1 \times 2.03$ mm, and the distance between the sheet edge and hole center was 19.05 mm. The specimen configuration is shown in Fig. 1. Based on optical measurements of the three specimens, the mean inner sheet hole diameter D_{hole} was 6.51 mm, and the rivet protruding height above the inner sheet surface, H_{o}, was 9.95 mm. The rivet shank diameter D was 6.35 mm, and the height was 14.29 mm. The mean clearance between the sheet hole and rivet shank was 0.08 mm.

Microstrain gauges made by Measurements Group, Raleigh, North Carolina were employed to capture strain variations during the test.[7,11,12] Gauges 1–4 were mounted on the inner sheet surface before riveting and used to capture the strain variation during the riveting process. Gauges 5–11 were mounted after riveting. All of the micro strain gauges were positioned in the joint longitudinal (joint tensile) direction as shown in Fig. 2. Microstrain gauges 1, 2, 10, and 11 were micro-measurements EA-13-031DE-350 type with a gauge factor of $2.06 \pm 1.0\%$ and transverse sensitivity of $(1.2 \pm 0.2)\%$ at

Received 9 June 2005; revision received 27 October 2005; accepted for publication 2 November 2005.

*Research Officer, Structures and Materials Performance Laboratory, Institute for Aerospace Research, 1200 Montreal Road; Gang.Li@nrc-cnrc.gc.ca. Member AIAA.

†Senior Research Officer, Structures and Materials Performance Laboratory, Institute for Aerospace Research, 1200 Montreal Road. Member AIAA.

‡Structures Group Leader, Structures and Materials Performance Laboratory, Institute for Aerospace Research, 1200 Montreal Road. Member AIAA.

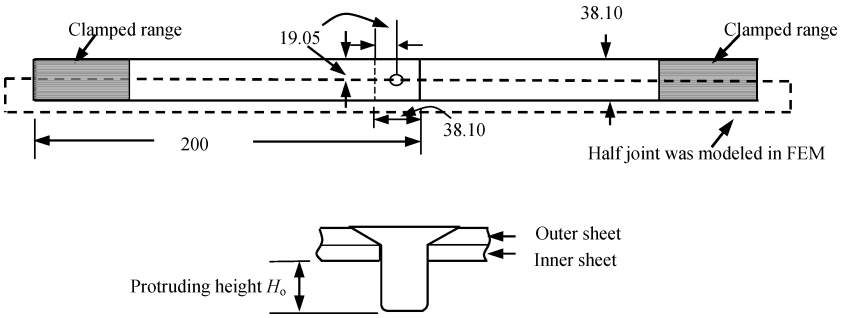

Fig. 1 Lap joint with single countersunk rivet (millimeters).

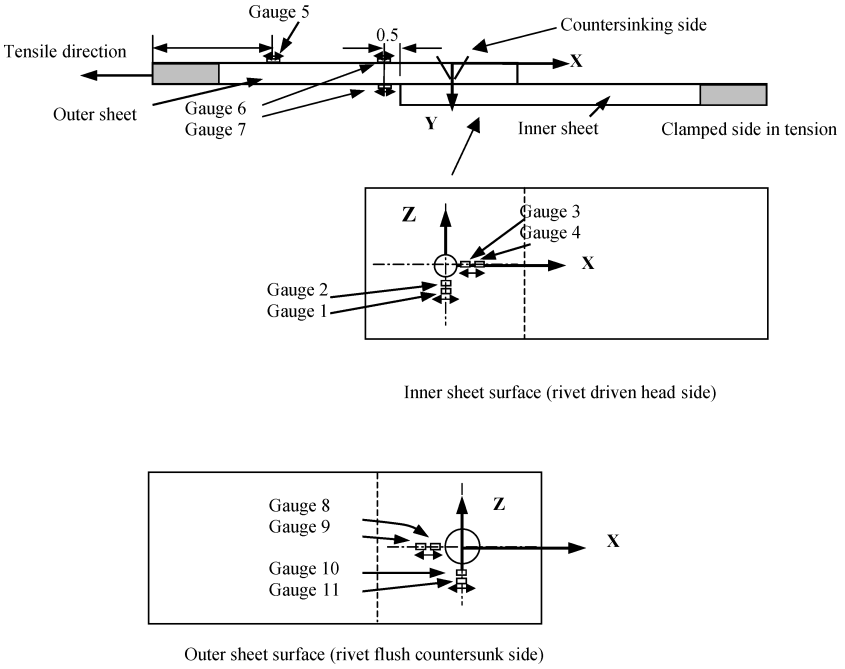

Fig. 2 Microstrain gauge arrangements in joint specimen (not to scale).

Table 1 Gauge location on the joint inner sheet surface of microstrain gauges 1–4[a]

Gauge	Position	Location, mm
1	z position ± 0.4[b]	10.3
2	Absolute value	8.7
3	x position ± 0.4[b]	8.7
4	x position ± 0.4[b]	10.4

[a]Rivet squeeze force 53.38 kN.
[b]Gauge length was approximately 0.8 mm and values were measured between hole center and gauge center positions.

Table 2 Locations of microstrain gauges 5–11[a]

Gauge	Position	Location
5	x position	81
6, 7	x position	19.6
8	x position ± 0.4	7.7
9	x position ± 0.4	9.4
10	z position ± 0.4	9.7
11	Absolute value	11.1

[a]Squeeze force 53.38 kN.
[b]Gauge location on the joint outer sheet surface.

24°C. Microstrain gauges 3–9 were micro-measurements EA-13-031EC-350 type with a gauge factor of $2.09 \pm 1.0\%$ and transverse sensitivity of $(0.4 \pm 0.2)\%$ at 24°C. Gauges 1 and 2 were used to measure hoop direction strains, and gauges 3 and 4 were used to measure radial strains during the riveting process. Gauges 1–11 were reset to zero and then used to measure the strain variations during the tensile loading stage.

To avoid possible damage to the strain gauges by the large rivet driven head deformation and actual difficulties in gauge setup, the strain gauges 1–4 were not mounted in the range of 2.5 mm to the hole edge. Tables 1 and 2 give the strain gauge locations. The gauges were in good conditions and also well calibrated before and after mounting. Because these gauges were not within the hole vicinity, the joint maximum remote tensile stress was less than one-third of the sheet initial yield stress. The measured strains were much lower than the strain gauge limit of approximately 3%. Thus, the influences of the gauge transverse sensitivity and nonlinearity on the measured strains should be minor and not considered. Each strain-gauged specimen was tested under one of the three different squeeze forces.[14] The coordinate frame origin position is at the hole center. Only the strain results obtained from the joint riveted using the 53.38-kN squeeze force were compared with the corresponding numerical predictions in this paper. Strain comparisons for the joints riveted using 35.59 and 44.48 kN are summarized elsewhere.[14]

B. Testing Equipment and Loading Condition

Lap joint specimens were riveted and then loaded in tension using a 250-kN MTS load frame, serial number 455 and model number 311.11.

To avoid both thermal and inertial effects on the material properties, a small constant load ramp of 111.2 N/s was chosen for all of the rivet installations,[11–14] which is much slower than that used

in the actual riveting process. The cyclic tensile testing parameters were as follows: a cyclic frequency of 0.04 Hz, a joint maximum remote tensile stress of 98.5 MPa, a stress ratio of 0.02, and a total of three tensile cycles used to load the joints. Tabs with dimensions of $40 \times 38.1 \times 2.03$ mm were used at the two far ends of the joint so that no initial secondary bending moment was induced before applying the tensile load. The microstrain gauges only captured the strain values in the initial half-cycle when the tensile load increased from zero to 98.5 MPa (Ref. 14) because these measured data were adequate for validation of numerical predictions.

III. Finite Element Simulations

A. Joint Dimensions and Material Parameters

Because of the symmetry of the joint configuration, only one-half of the joint (Fig. 1) was modeled. Symmetric boundary conditions were applied to the joint center plane along the longitudinal direction.

An isotropic hardening behavior was assumed for both the rivet and sheet materials. The material constants C and m were calculated by substituting the uniaxial tensile test data[12] into Eq. (1):

$$\sigma_{\text{true}} = C(\varepsilon_{\text{true}})^m \tag{1}$$

The true stress and plastic strain values were entered into the table provided by the MSC. Patran interface, which uses linear interpolation for values between the points to implement the hardening behavior in the model.

Material parameters for the 2117-T4 Al alloy MS20426AD8-9 rivet[4,15] and 2024-T3 Al alloy bare sheet[11–15] are summarized in Tables 3 and 4, respectively. The ε_y was the initial yield strain and $\varepsilon_{\text{true}}$ was the true strain.

Table 3 Elastic and plastic properties for 2117-T4 Al alloy MS20426AD8-9 rivet material

Parameter of rivet	Value
Young's modulus	71.7 GPa
Poisson's ratio	0.33
Initial yield stress σ_y	172 MPa
Hardening parameters when $0.02 \le \varepsilon_{\text{true}} \le 0.10$	$C = 544$ MPa and $m = 0.23$
Hardening parameters when $0.10 < \varepsilon_{\text{true}} \le 1.0$	$C = 551$ MPa and $m = 0.15$

B. Finite Element Modeling

The finite element (FE) model was generated in accordance to the experimental joints using the FE software packages MSC.Patran (pre- and postprocessor) version 2003r2 and MSC.Marc (solver) version 2001. A total of 7431 nodes and 5560 eight-noded three-dimensional reduced integration brick elements (type 117) were used and the three-dimensional FE model is shown in Fig. 3. Element type 117 is an eight-node isoparametric arbitrary hexahedral for general three-dimensional applications using reduced integration. This element uses an assumed strain formulation written in natural coordinates that ensures good representation of the shear strains in the element. This element is preferred over high-order elements when used in a contact analysis.[16]

Three deformable contact bodies, two sheets and one rivet, and two rigid contact bodies, a rigid pusher and a rigid set, were defined in the model. One rigid set contacted the joint bottom surface and the other rigid pusher was used to squeeze the rivet driven head. Specific contact pairs for both surface-to-surface and point-to-point were not needed because the current FE software package could handle this particular contact situation if it occurred. A friction coefficient of 0.2, based on corresponding experiments,[4] was used in the coulomb model for all contact surfaces.[4,11,13,14] A force-controlled riveting method was used in the current numerical study. Three different squeeze forces, 35.59, 44.48, and 53.39 kN, were applied to rivet the joints. After riveting, these joints were loaded in tension up to a remote stress of 98.5 MPa.

Multiple load steps with their specific boundary conditions were defined in one simulation. Load step 1 applied the squeeze force to the pusher, which would install the rivet; load step 2 released the

Table 4 Material parameters for 2.03-mm-thick 2024-T3 Al alloy bare sheet

Parameter of 2024-T3 Al alloy bare sheet	Value
Young's modulus	72.4 GPa
Poisson's ratio	0.33
Initial yield stress σ_y	310 MPa
True ultimate stress	552 MPa
Hardening parameters when $\varepsilon_y \le \varepsilon_{\text{true}} \le 0.02$	$C = 676$ MPa and $m = 0.14$
Hardening parameters when $0.02 < \varepsilon_{\text{true}} \le 0.1$	$C = 745$ MPa and $m = 0.164$
Slope of linear hardening curve when $\varepsilon_{\text{true}} > 10\%$	1034 MPa

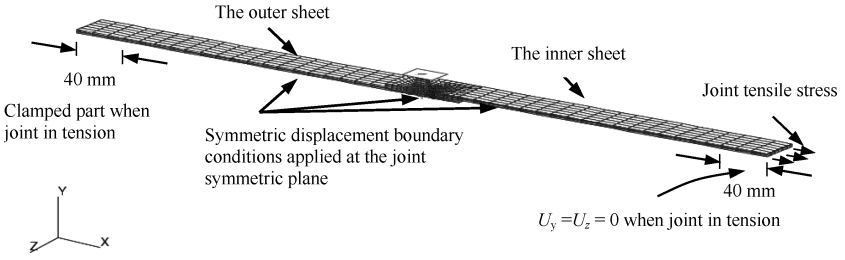

a) Three-dimensional FE model

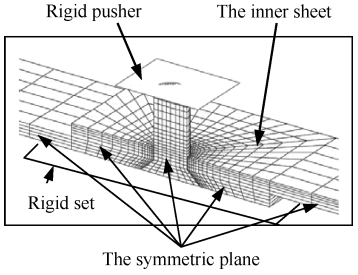

b) Close view of rivet region with two rigid bodies

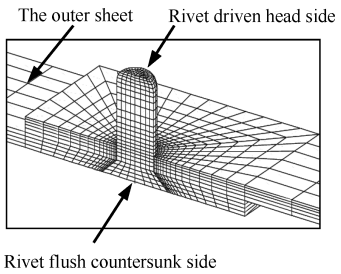

c) Rivet region after removal of two rigid bodies

Fig. 3 FE model of joint with one rivet meshed using total of 5560 eight-node reduced integration brick elements and 7431 nodes.

squeeze force back to 0; and, finally, load step 3 applied the in-plane loading to the joint up to a maximum stress of 98.5 MPa. In the final load step, the three deformable bodies contacted each other whereas the rigid bodies were deactivated.

C. Displacement Boundary Conditions Used in Three-Dimensional FE Model

As shown in Fig. 3, the following displacement boundary conditions were used during the riveting process:

For set 1, $U_y = U_z = 0$ was at the remote edges of the joint.

For set 2, $U_x = U_z = 0$ was applied to the rivet axis.

For set 3, $U_z = 0$ was applied at the joint longitudinal center plane.

The influence of the boundary conditions at the joint far ends, set 1, on the stress and strain distributions in the hole vicinity during the riveting process can be ignored based on the Saint-Venant's principle (see Ref. 17).

The following displacement boundary conditions were used in the tensile loading stage after the squeeze forces were released:

For set 4, the displacements, $U_x = U_y = U_z = 0$, were applied at the joint left far end for a length of 40 mm. The length of the clamped joint end was 40 mm in the experiments.

For set 5, displacements, $U_y = U_z = 0$, were applied at the joint right far end for a length of 40 mm, and the joint was loaded in tension in the longitudinal x direction.

For set 6, $U_z = 0$ was applied at the joint symmetric (center) plane in longitudinal direction (x axis).

IV. Results and Discussion

A. Joint Deformations

The deformations obtained from the experimental and numerical results are shown in Figs. 4 and 5. During the experimental testing, the rivets installed using 35.59- and 44.48-kN squeeze forces were sheared off when the remote tensile stress was 97.3 MPa (load was 7.53 kN) within the initial half-cycle of the tensile stage. The two rivet shanks were fully fractured, and one of the fractured surfaces is shown in Fig. 4c. Dimples were present over most of the fracture surface, but a small smooth area was also present. It could be deduced that the outer sheet sharp knife-edge generated this smooth area by cutting into the rivet and then an overload occurred under both the shear and tension loading conditions. The joint riveted using 53.38 kN did not fail during the tensile test. The large shear/cut deformation location in rivets can be clearly observed in Figs. 4 and 5, which was consistent with the experiments. Results showed that the numerical simulations provided reasonable joint deformations.

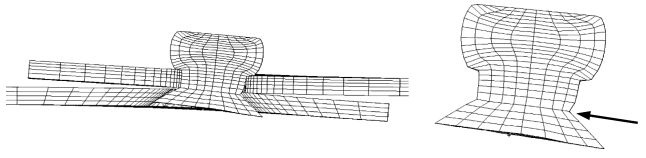

a) FE prediction for joint and rivet deformations with tensile load of 98.5 MPa after releasing 35.59-kN squeeze force

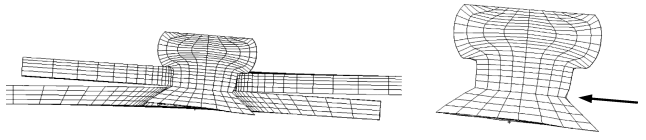

b) FE prediction for joint and rivet deformations with tensile load of 98.5 MPa after releasing 44.48-kN squeeze force

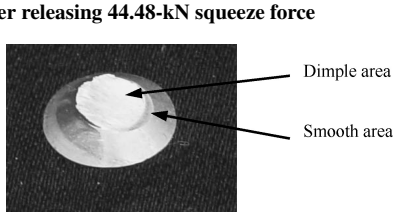

c) Fracture surface of rivet installed using 44.48-kN squeeze force after tensile load in joint was 97.3 MPa

Fig. 4 Joints in tension after releasing two different rivet squeeze forces obtained from numerical models and rivet fracture surface obtained from experimental tests; arrow points to rivet large shear/cut location.

Table 5 Comparison of MS20426AD8-9 rivet driven head deformation ratio of D_{max}/D

Squeeze force, kN	D_{max}/D FE result	D_{max}/D Experimental result	Empirical prediction of D_{max}/D Eq. (1a) (Ref. 12)	Empirical prediction of D_{max}/D Eq. (5) (Ref. 12)
35.59	1.51	1.50	1.48	1.50
44.48	1.62	1.61	1.60	1.61
53.38	1.72	1.70	1.71	1.71

Table 6 Comparison of MS20426AD8-9 rivet driven head deformation of H

Squeeze force, kN	FE result, mm	Experimental result, mm	Empirical prediction, Eq. (1b) (Ref. 12), mm
35.59	4.53	4.61	4.68
44.48	3.90	4.01	4.01
53.38	3.42	3.53	3.54

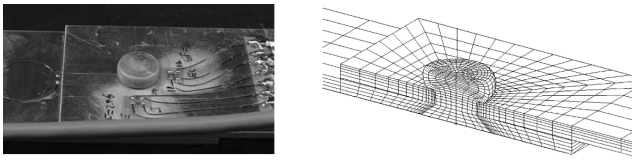

a) Rivet installed using 53.38-kN squeeze force obtained from experimental and numerical results

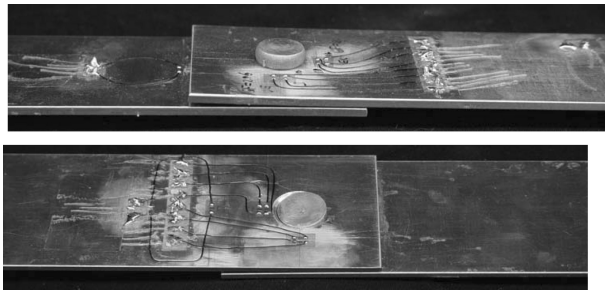

b) Joint deformation after experimental tensile test

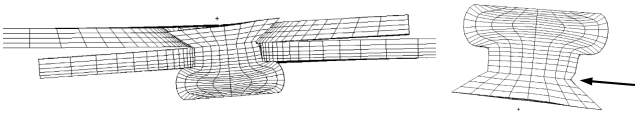

c) Joint loaded in tension to 98.5 MPa after releasing 53.38-kN squeeze force as predicted by FE simulations

Fig. 5 Joints in tension after releasing the two different rivet squeeze forces obtained from numerical models and rivet fracture surface obtained from experimental tests; arrow points to rivet large shear/cut location.

Comparisons of the experimental and numerical results as well as empirical predictions for D_{max}/D and H after releasing the squeeze force are given in Tables 5 and 6. Where D is the rivet shank diameter, D_{max} is the maximum shank diameter, and H is the rivet driven head height above the joint inner sheet surface after riveting. Large squeeze forces induced large driven head deformations. A good agreement was achieved for the rivet driven head deformation from the numerical simulations as shown in Tables 5 and 6. The resulting interferences between the rivet and the coupon hole were studied numerically using a fine mesh in an axisymmetric two-dimensional FE model and can be found elsewhere.[11]

B. In Situ Quantitative Comparisons Between the Experimental and Numerical Results

1. Riveting Process

Comparisons of the rivet driven head compressive displacement vs the squeeze force during the riveting process obtained from the

experimental and numerical results are presented in Fig. 6. Good agreement was achieved between the two techniques. The maximum relative error between the numerical predictions and experimental data for rivet driven head displacement was approximately −9% during the rivet installation. However, the difference in the rivet driven head displacement was smaller at the end of the riveting process, about −5%, as shown in Fig. 6. In Fig. 6, there appears to be some elastic recovery in the experiments, which is relatively small in the numerical simulations.

Comparisons of the strain variations in gauges 1–4 during the riveting process using the 53.38-kN squeeze force are present in Fig. 7. The hoop/tangential strain was tensile during the riveting process whereas the radial strain was compressive. Again, a very limited elastic recovery in the numerical simulations for these strains is observed in Fig. 7.

The experimental strain variations were similar to the results in Refs. 7, 11, and 12. The strain reversal values were larger than the earlier test results,[11,12] which could have resulted from the clearance that was present between the sheet/rivet hole interface as well as the rivet standing position (distance of rivet head above sheet surface) during the riveting process. A similar trend without the large strain reversal can be observed in the numerical results. The difference between the numerical predictions and experimental results was smaller after riveting. For example, due to the reversal strain situation, a large difference in strain for gauge 1 occurred at the squeeze force of approximately −27 kN during the riveting process and the difference was approximately 3E-04 strain after riveting. The riveting process with the strain reversal variations are discussed elsewhere.[18]

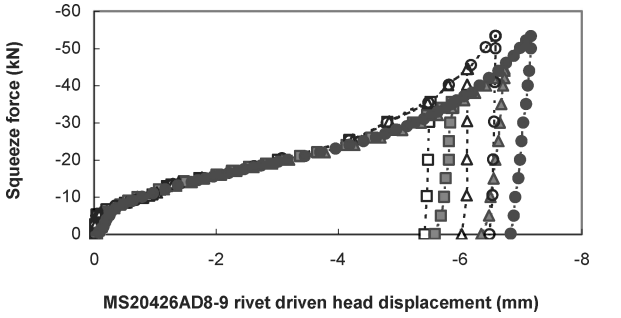

Fig. 6 Comparisons of MS20426AD8-9 rivet driven head displacements obtained from experimental and numerical results in riveting process under three different squeeze forces: - - □ - -, FE, F = 35.59 kN; - - △ - -, FE, F = 44.48 kN; - - ○ - -, FE, F = 53.38 kN; - - ■ - -, experiment, F = 35.59 kN; - - ▲ - -, experiment, F = 44.48 kN; and - - ● - -, experiment, F = 53.38 kN.

2. *Comparisons of Strains During Tensile Loading Stage*

To compare the experimental and numerical results during the tensile loading stage, the experimentally measured residual strains were added to the corresponding gauge values for gauges 1–4 during the tensile loading stage. Gauges 8–11 were mounted after the riveting process so that there were no residual strains present. The residual strain values obtained from the numerical simulations were added to their corresponding values of gauges 8–11 during the tensile loading stage.

Figures 8 and 9 present the comparisons in the strain variations during the tensile loading stage obtained from both the experimental and numerical results. Note from Figs. 8 and 9 that good agreement was achieved between these results for all of the strain pairs. The tensile residual hoop strain values present in Figs. 8 and 9 were induced during the riveting process. It can be observed from Figs. 8 and 9 that the hoop strain values in gauges 1, 2, 10, and 11 changed from tensile to compressive with increasing tensile loading, which was observed for both the experimental and FE results. As expected, the load path eccentricity caused secondary bending when the riveted lap joints were in tension, as shown in Fig. 10. Compressive strains in gauges 1, 2, 10, and 11 that were located on the sheet surfaces were generated by these joint lateral deflections.

As expected, the rivet squeeze force did not influence the joint remote strain variations. The longitudinal strain variations in gauge 5 for the three joints were very close to the FE results, as shown in Fig. 11. The remote strain was within the elastic range of the material.

Strain gauges 6 and 7 were mounted near the joint overlap end to measure the longitudinal strain values at the outer sheet upper and lower surfaces, which were used to estimate the secondary bending moment. Comparisons of the longitudinal strain variations in these gauges between the experimental and numerical results are present in Fig. 12. Good agreement was achieved between the experimental and numerical results. The relative errors between the numerical and experimental strain results were 1% in gauge 6 and −5% in gauge 7 when the remote tensile stress was 98.5 MPa.

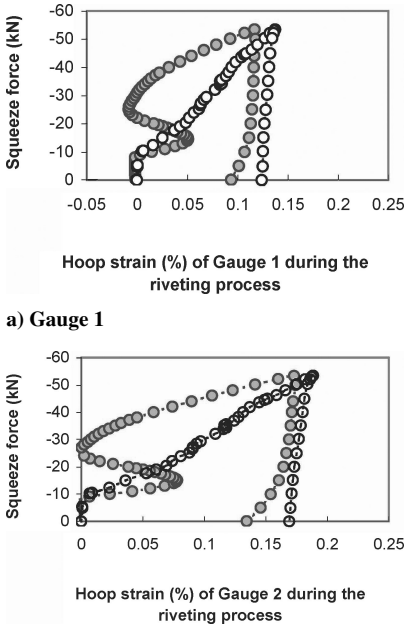

Fig. 7 Comparison of strain variations in gauges 1–4 on joint inner sheet surface during riveting process using 53.38-kN squeeze force: - - ● - -, experimental result and - - ○ - -, FE prediction.

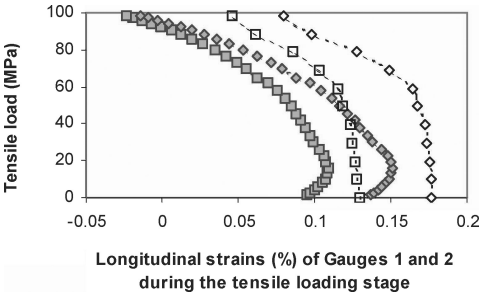

a) Gauges 1 and 2

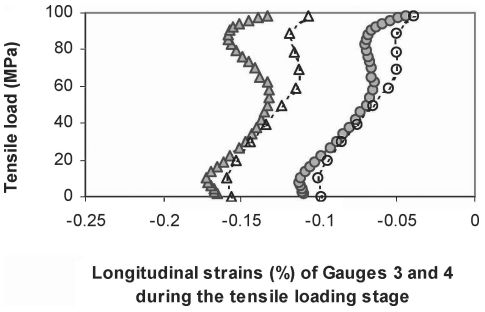

b) Gauges 3 and 4

Fig. 8 Comparison of strain variations in gauges 1–4 during tensile loading stage of joint after releasing 53.38-kN squeeze force: - - ■ - -, experiment, gauge 1; - - ◆ - -, experiment, gauge 2; - - ▲ - -, experiment, gauge 3; - - ● - -, experiment, gauge 4; - - □ - -, FE, gauge 1; - - ◇ - -, FE gauge 2; - - △ - -, FE gauge 3; and - - ○ - -, FE gauge 4.

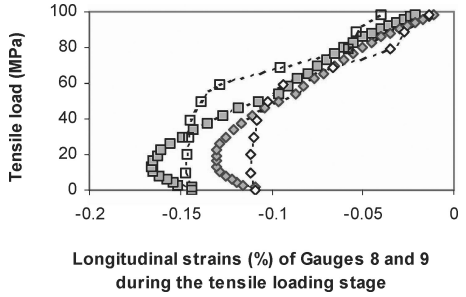

a) Gauges 8 and 9

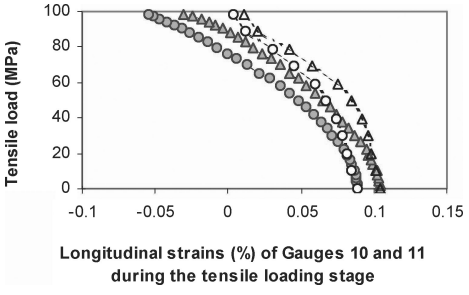

b) Gauges 10 and 11

Fig. 9 Comparison of strain variations in gauges 8–11 during tensile loading stage of joint after releasing 53.38-kN squeeze force: - - ■ - -, experiment, gauge 8; - - ◆ - -, experiment, gauge 9; - - ▲ - -, experiment, gauge 10; - - ● - -, experiment, gauge 11; - - □ - -, FE gauge 8; - - ◇ - -, FE gauge 9; - - △ - -, FE gauge 10; and - - ○ - -, FE gauge 11.

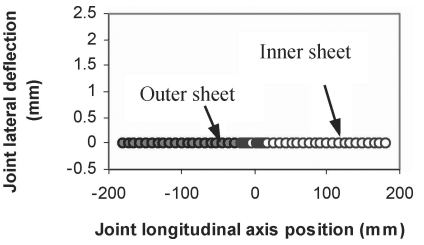

a) Before tension

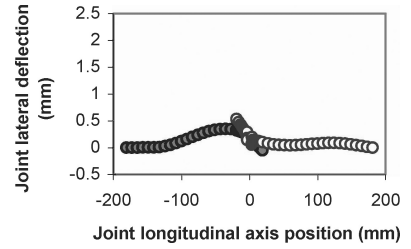

b) Tensile stress of 9.85 MPa

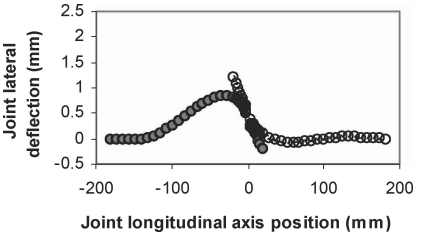

c) Tensile stress of 49.25 MPa

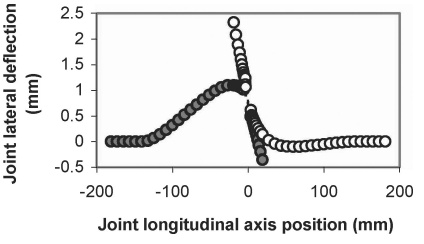

d) Tensile stress of 98.5 MPa

Fig. 10 Joint lateral (sheet thickness) direction deflections when loaded in tension using different tensil loads as predicted by three-dimensional FE analysis.

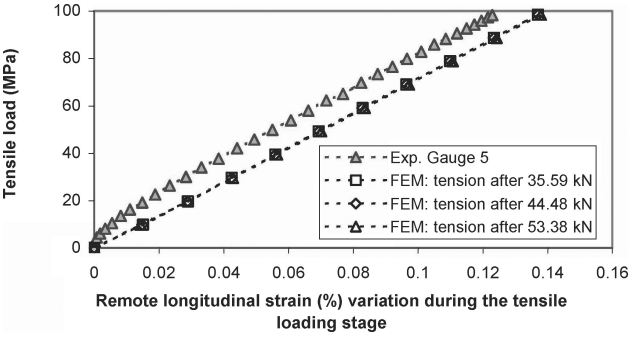

Fig. 11 Comparisons of remote strain variations in gauge 5 during tensil loading stage of joints after releasing three different squeeze forces.

It could be drawn from these strain comparisons that residual stress induced by the riveting process and stress conditions during the joint tensile loading stage could be analyzed using the current numerical results with reasonable accuracy.

The discrepancy between the experimental and FE predictions could be explained by the following: 1) inaccuracies in the constitutive models beyond yielding for the sheet and rivet used in the FE model; 2) perfect assumptions made for the material properties and perfect geometry surface; 3) difference in how the strain values were obtained and the strain was determined from a point/node in the FE model while it was averaged over the gauge area for the experiments; 4) numerical errors in the FE model, for example, insufficiently refined FE meshes and inaccurate results; and 5) errors associated with the strain gauge, for example, gauge reliability and gauge mount conditions.

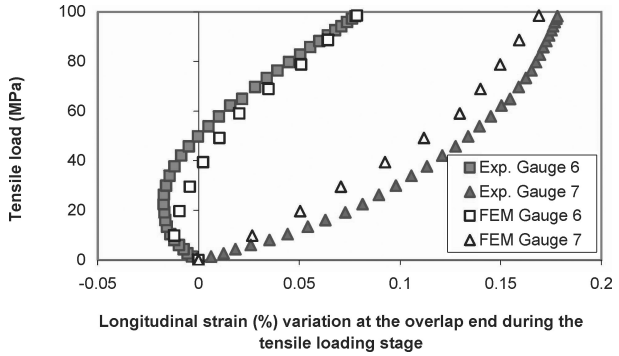

Fig. 12 Strain variations in gauges 6 and 7 near joint overlap end during tensil loading stage after releasing 53.38-kN rivet squeeze force obtained from experimental and FE results.

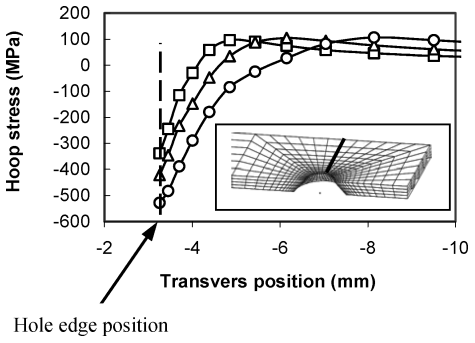

a)

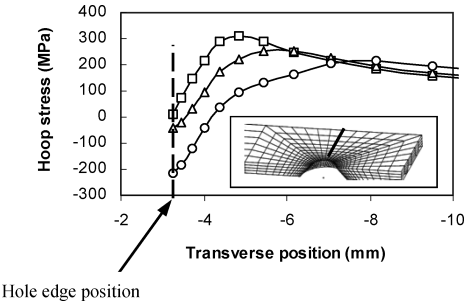

b)

Fig. 13 Hoop stress variations along transverse path on outer sheet faying surface when tensile load was a) 0 MPa and b) 59.1 MPa after releasing three different squeeze forces: - - -□- - -, riveted using 35.59-kN squeeze force; - - -△- - -, riveted using 44.48-kN squeeze force; and - - -○- - -, riveted using 53.38-kN squeeze force.

C. Hoop Stress Variations Along Prescribed Transverse Path

Crack nucleation usually first occurs in the fastener hole vicinity on the outer sheet faying surface during fatigue tests. Hoop stress conditions in the fastener hole vicinity along transverse path on the outer sheet faying surface would be a major stress component to cause crack nucleation and then growth. Provided the strain gauges could not be mounted on the fastener hole vicinity, the study of the hoop stress variation in the fastener hole vicinity along the transverse path could be necessary to evaluate right and accurate numerical results. Hoop stress variations in the tensile loading stage along a prescribed transverse path on the faying surface of the outer sheet were studied from the FE solutions. This path was perpendicular to the joint longitudinal tensile direction.

The details of the numerical analysis used to achieve consistent results are provided elsewhere.[19] Figure 13 presents the hoop stress variations along the transverse path under two different tensile loads, 0 and 59.1 MPa. The hoop stresses in Fig. 13a were the residual stresses after the riveting process. Large rivet squeeze forces generated larger compressive residual stresses. The results in Fig. 13 show that the residual stresses induced by the rivet squeeze force have a considerable effect on the stress variations in the tensile loading stage.

Nonlinear variations in the hoop stress along the prescribed path can be observed. When the hoop stress variations under the different joint tensile loads are compared, consistent and compatible results for the hoop stress can be achieved using the current FE model when the joint tensile stress was up to 59.1 MPa, 60% of the highest stress of 98.5 MPa. This stress value is significantly higher than the maximum nominal tensile stress of 32.8 MPa that is present at each rivet in a three-row rivet lap joint.[9] Thus, the numerical results under the 59.1-MPa remote tensile stress condition could provide more insight into the stress conditions in the hole vicinity than that under three-row rivet lap joints.

When the joint remote tensile stress was beyond 59.1 MPa (Ref. 19), a large load transfer between the sheet and rivet led to the occurrence of the incompatible hoop stresses in the fastener hole vicinity obtained from the numerical models. Accordingly, these numerical results for stresses, the hoop stress in the hole vicinity along the transverse path, and full-field stress contours, were not considered further.

D. Full-Field Stress Contours

The maximum principal stress is one of the most important components in the study of crack nucleation of fuselage lap joints. Crack nucleation usually occurs in the outer sheet. The corresponding full-field contours of the residual minimum principal stress after the riveting process and maximum principal stress when the joints were loaded in tension are presented in Figs. 14 and 15, respectively, highlighting the rivet hole in the outer sheet. Nonlinear stress distributions are shown in Figs. 14 and 15.

Figure 14 shows the full-field contours of the residual minimum principal stress induced by the riveting process. It can be seen in Fig. 14 that 1) large compressive residual stresses are present the area in the hole vicinity and 2) the compressive area increased with the increment of the squeeze forces. The full-field stress contours of the maximum principal stress, when the joints were in tension, are present in Fig. 15. Two results can be observed from Fig. 15: 1) The distribution area and shape of the maximum principal stress shifted to the hole upper side as labeled in Fig. 15c. 2) The maximum

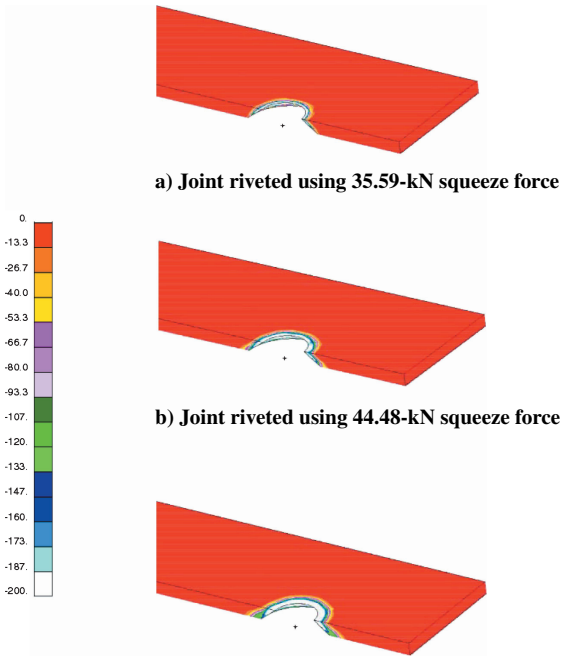

a) Joint riveted using 35.59-kN squeeze force

b) Joint riveted using 44.48-kN squeeze force

c) Joint riveted using 53.38-kN squeeze force

Fig. 14 Full-field contours of residual minimum principal stress (megapascal) on faying surface of outer sheet after riveting process using three different squeeze forces.

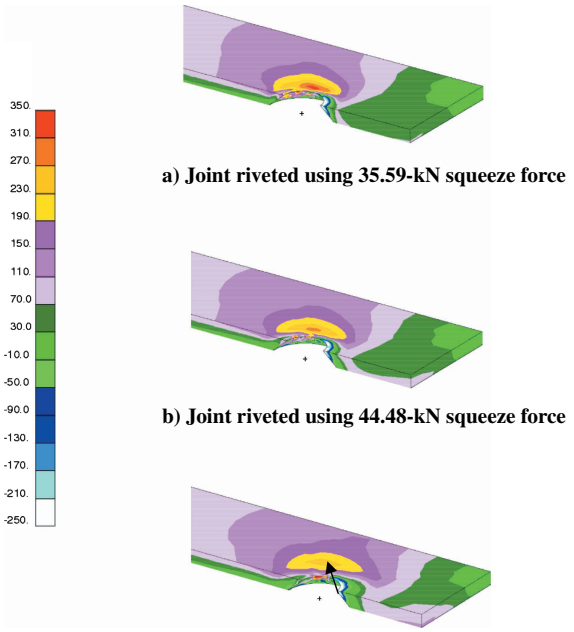

a) Joint riveted using 35.59-kN squeeze force

b) Joint riveted using 44.48-kN squeeze force

c) Joint riveted using 53.38-kN squeeze force

Fig. 15 Full-field contours of maximum principal stress (megapascal) on faying surface of outer sheet when joint was loaded in tension by remote stress of 59.1 MPa after riveting process; arrow shows high maximum principal stress position.

principal stress magnitude decreased with the larger rivet squeeze force when the joints were loaded in tension. The large maximum principal stress distribution area and shape when the joints were loaded in tension were consistent with the experimental results.[8]

V. Conclusions

The following conclusions can be drawn from this study:

1) Experimental tests of lap joints with one countersunk type rivet were carried out from the riveting process to the tensile loading stage. The joint riveted using the 53.38-kN squeeze force had a higher tensile strength than the other two joints riveted using 35.59- and 44.48-kN squeeze forces. Experimental results showed that the tensile strength of the single-row countersunk riveted lap joints was controlled by the rivet failures in two instances. To improve the joint integrity strength, the knife edge in the outer sheet hole should be avoided by using a proper size rivet in the joint design. A three-dimensional FE model was developed to simulate the experimental procedures.

2) Variations in the compressive displacement of the rivet driven head vs squeeze force during the riveting process were captured. In situ strain values were measured using microstrain gauges during the entire loading sequence. Good agreement was achieved between the experimental and numerical results in both the riveting process and tensile loading stage. The residual stress and strain induced by the riveting process were numerically predicted. The stress and strain variations in the tensile loading stage considering the effects of the residual stress/strain were investigated.

3) Consistent and compatible behaviors of the hoop stress variations along the outer sheet prescribed paths were observed when the tensile load was less than or equal to 60% of the highest stress of 98.5 MPa. The numerical results showed that the residual stress induced by the rivet squeeze force had a considerable effect on the stress variations in the tensile loading stage.

4) Full-field contours for the residual minimum principal stress induced by the riveting process and maximum principal stress when joints were loaded in tension were presented. Nonlinear stress distributions can be observed from these full-field contours. Large rivet squeeze forces moved the high maximum principal stress away from the joints hole vicinity.

Acknowledgments

This work has been carried out under Institute for Aeronautical Research Program 303 Aerospace Structures, Project 46_QJ0_37, Residual Stress in Riveted Lap Joints. The financial assistance received from Department of National Defence (DND)/Defence Research and Development Canada (DRDC) is gratefully acknowledged. Our sincere thanks to J. P. Komorowski, and G. Eastaugh for their valuable discussions, suggestions, and help in the research. Many thanks to those people who have, in one way or another, contributed to this work.

References

[1]Müller, R. P. G., "An Experimental and Analytical Investigation on the Fatigue Behavior of Fuselage Riveted Lap Joints," Ph.D. Dissertation, Faculty of Aerospace Engineering, Delft Univ. of Technology, Delft, The Netherlands, Oct. 1995.

[2]Fung, C.-P., and Smart, J., "An Experimental and Numerical Analysis of Riveted Single Lap Joints," *Proceedings of the Institution of Mechanical Engineers, Part G, Journal of Aerospace Engineering*, Vol. 208, No. 2, 1994, pp. 79–90.

[3]Fung, C.-P., and Smart, J., "Riveted Single-Lap Joints. Part 1: A Numerical Parametric Study," *Proceedings of the Institution of Mechanical Engineers, Part G, Journal of Aerospace Engineering*, Vol. 211, No. 1, 1997, pp. 13–27.

[4]Szolwinski, M. P., and Farris, T. N., "Linking Riveting Process Parameters to the Fatigue Performance of Riveted Aircraft Structures," *Journal of Aircraft*, Vol. 37, No. 1, 2000, pp. 130–137.

[5]Trego, A., and Cope, D., "Evaluation of Damage Tolerance Analysis Tools for Lap Joints," *AIAA Journal*, Vol. 39, No. 12, 2001, pp. 2250–2254.

[6]Li, G., and Shi, G., "Residual Stresses in Riveted Lap Joints: A Literature Review," Inst. for Aerospace Research, LTR-SMPL-2002-0019, National Research Council Canada, 2002.

[7]Langrand, B., Patronelli, L., Deleotombe, E., Markiewicz, E., and Drazetic, P., "An Alternative Numerical Approach for Full Scale Characterization for Riveted Joint Design," *Aerospace Science and Technology*, Vol. 6, No. 5, 2002, pp. 343–354.

[8]Eastaugh, G. F., Straznicky, P. V., Krizan, D. V., Merati, A. A., and Cook, J., "Experimental Study of the Effects of Corrosion on the Fatigue Durability and Crack Growth Characteristics of Longitudinal Fuselage Splices," *Proceedings of the Fourth DoD/FAA/NASA Aging Aircraft Conference*, May 2000.

[9]Bellinger, N. C., Komorowski, J. P., and Benak, T. J., "Residual Life Prediction of Corroded Fuselage Lap Joints," *International Journal of Fatigue*, Vol. 23, Supplement No. 1, 2001, pp. S349–S356.

[10]Mackerle, J., "Finite Element Analysis of Fastening and Joining: A Bibliography (1990–2002)," *International Journal of Pressure Vessels and Piping*, Vol. 80, No. 4, 2003, pp. 253–271.

[11]Li, G., and Shi, G., "Effect of the Riveting Process on the Residual Stress in Fuselage Lap Joints," *Canadian Aeronautics and Space Journal*, Vol. 50, No. 2, 2004, pp. 91–105.

[12]Li, G., and Shi, G., "Investigation of Residual Stress in Riveted Lap Joints: Experimental Study," Inst. for Aerospace Research, LTR-SMPL-2003-0099, National Research Council Canada, 2003.

[13]Li, G., and Shi, G., "Neutron Diffraction Measurement and FE Simulation of Residual Strains and Stress in Fuselage Lap Joints," Inst. for Aerospace Research, LTR-SMPL-2004-0003, National Research Council Canada, 2004.

[14]Li, G., and Shi, G., "Investigation of Residual Stress/Strain in Lap Joints with a Single Countersunk Rivet," Inst. for Aerospace Research, LTR-SMPL-2004-0130, National Research Council Canada, 2004.

[15]"Metallic Material and Elements for Aerospace Vehicle Structures," MIL-HDBK-5H, U.S. Dept. of Defense, Dec. 1998.

[16]"MARC Volume B: Element Library, Version K7," MARC Analysis Research Corp., Palo Alto, CA, Aug. 1997.

[17]Timoshenko, S. P., and Goodier, J. N., *Theory of Elasticity*, 3rd ed., McGraw–Hill, 1970, Chap. 3.

[18]Langrand, B., Patronelli, L., Deleotombe, E., Markiewicz, E., and Drazetic, P., "Full Scale Experimental Characterization for Riveted Joint Design," *Aerospace Science and Technology*, Vol. 6, No. 5, 2002, pp. 333–342.

[19]Li, G., and Shi, G., "Evaluation of the Numerical Modeling Results in Simulating the Fuselage Lap Joints with a Single Countersunk-Type Rivet," Inst. for Aerospace Research, LM-SMPL-2004-0118, National Research Council Canada, 2004.